The Thesis Committee for Travis Collin Turner
Certifies that this is the approved version of the following thesis:

Synthesis, Characterization, and Oxygen Evolution Reaction Catalysis of Nickel-Rich Oxides

APPROVED BY
SUPERVISING COMMITTEE:

Supervisor:

Arumugam Manthiram

Guihua Yu

Synthesis, Characterization, and Oxygen Evolution Reaction Catalysis of Nickel-Rich Oxides

by

Travis Collin Turner, B.S.Ch.

Thesis

Presented to the Faculty of the Graduate School of
The University of Texas at Austin
in Partial Fulfillment
of the Requirements
for the Degree of

Master of Science in Engineering

The University of Texas at Austin
May 2014

Acknowledgements

I would like to thank my advisor, Professor Arumugam Manthiram, for enabling me to continue my graduate education in his research group. I would also like to thank Professor Guihua Yu for being my thesis reader.

I am indebted to Zachary Moorhead-Rosenberg and Karl Kreder for showing how to prepare and test coin cell batteries. I am also grateful to Veronica Augustyn for helping me with ORR/OER testing and data analysis.

Abstract

Synthesis, Electrochemical Characterization, and Oxygen Evolution Reaction Catalysis of Nickel-Rich Oxides

Travis Collin Turner, M.S.E.
The University of Texas at Austin, 2014

Supervisor: Arumugam Manthiram

A successful transition from fossil fuels to renewable energies such as wind and solar will require the implementation of high-energy-density storage technologies. Promising energy storage technologies include lithium-ion batteries, metal-air batteries, and hydrogen production via photoelectrochemical water splitting. While these technologies differ substantially in their mode of operation, they often involve transition-metal oxides as a component. Thus, fundamental materials research on metal oxides will continue to provide much needed advances in these technologies.

In this thesis, the electrochemical and electrocatalytic properties of Fe- and Mn-substituted layered $LiNiO_2$ materials were investigated. These materials were prepared by heating mixed nitrate precursors in O_2 atmosphere at 700-850 ^{o}C for 12 h with intermediate grindings. The products were chemically delithiated with NO_2BF_4, and the delithiated samples were annealed at moderate temperatures in order to transform them to a spinel-like phase. Samples were characterized by inductively coupled plasma analysis and Rietveld refinement of the X-ray diffraction patterns, which were found to be in reasonably close agreement regarding lithium stoichiometry. Spinel-like materials were found to possess an imperfect spinel structure when heated at lower temperatures and a significant amount of NiO impurity was formed when heated to higher temperatures. This structural disorder was manifested during electrochemical cycling – only Mn-rich compositions showed reversible capacities at a voltage of around 4.5 V. The layered materials exhibited significant capacity loss upon cycling, and this effect was magnified with increasing Fe content.

These materials were further investigated as catalysts for the oxygen evolution reaction (OER). All samples containing Mn exhibited low OER activity. In addition, delithiation degraded catalyst performance and moderate temperature annealing resulted in further degradation. Because delithiation significantly increased surface area, activities were compared to the relative to BET surface area. $Li_{0.92}Ni_{0.9}Fe_{0.1}O_2$ exhibited significantly higher catalytic activity than $Li_{0.89}Ni_{0.7}Fe_{0.3}O_2$. This prompted testing of $Li_xNi_{1-y}Fe_yO_2$ (y = 0, 0.05, 0.1, 0.2, and 0.3) samples. It was found that a Fe content of approximately 10% resulted in the highest OER activity, with decreased activities for both larger and smaller Fe contents. These results were found to be consistent with studies of Fe substituted nickel oxides and oxyhydroxides, suggesting a similar activation mechanism.

Table of Contents

List of Tables

List of Figures

Chapter 1: Introduction

1.1 INTRODUCTION & MOTIVATION

The United States Energy Information Administration (EIA) publishes an annual *International Energy Outlook* (*IEO*). In its latest iteration, *IEO2013* projects a growth in world energy consumption of 56 percent between 2010 and 2040.[1] This equates to an increase from 524 quadrillion Btu annually to 820 quadrillion Btu annually. With increasing concerns of the deleterious environmental impacts of fossil fuels, this demand must be met with the addition of clean energy sources. Indeed, renewable energy and nuclear power are projected to be the fastest growing energy sources, increasing at a rate of 2.5 percent per year.

A successful transition from fossil fuels to renewable energies such as wind and solar will require the implementation of high-energy-density storage technologies. In automobiles, fuel cells or batteries must compete with the exceptionally high energy density of gasoline to provide reasonable ranges in between refueling or charging.[2] In power grids, cost-effective energy storage is required to compensate for temporal mismatch between production and consumption.[3] Promising energy storage technologies include lithium-ion batteries, metal-air batteries, and hydrogen production via photoelectrochemical water splitting. While these technologies differ substantially in their mode of operation, they often require transition-metal oxide components for their operation. Thus, fundamental materials research on metal oxides will continue to provide much needed advances in these technologies.

1.2 LITHIUM-ION BATTERIES

Lithium-ion batteries, envisaged by Whittingham in the mid-1970s,[4] became a reality with the discovery of practical cathodes, anodes, and electrolytes. Especially, notable advances have included the discovery of layered $LiCoO_2$ as a cathode intercalation material by Goodenough and Mizushima in 1979,[5] the replacement of lithium metal with graphite as the anode by Yazami in 1980,[6] and the assembly of a complete Li-ion cell incorporating these two electrodes by Yoshino in 1985.[7] These and other developments have made lithium-ion batteries ubiquitous in modern electronics. In addition to providing portable power to countless numbers of notebook computers, mobile phones, and tablets, lithium-ion batteries have recently become the power supply of choice for modern electric vehicles.[8] A discussion of issues with current lithium-ion battery technology first requires an explanation of their design and operation.

1.2.1 Design & Operating Principles

Although many lithium-ion battery reviews exist in the literature,[9-12] this summary will focus on basic operating principles and the two main cathode materials that are currently used. As electrochemical devices, lithium-ion batteries consist of two electrodes (a cathode and an anode), an electrolyte, and a separator. These components are shown in Figure 1.1. The most widely used cathode at this time is layered $LiCoO_2$, while graphite serves as the anode. The electrolyte is typically an organic solvent with dissolved lithium salts. When a battery is fully discharged, there are no lithium ions in the anode and the cathode has unit lithium stoichiometry. Upon charging, lithium ions migrate from the cathode to the graphite anode via the electrolyte. Simultaneously, electrons flow from the cathode to the anode through an external circuit.

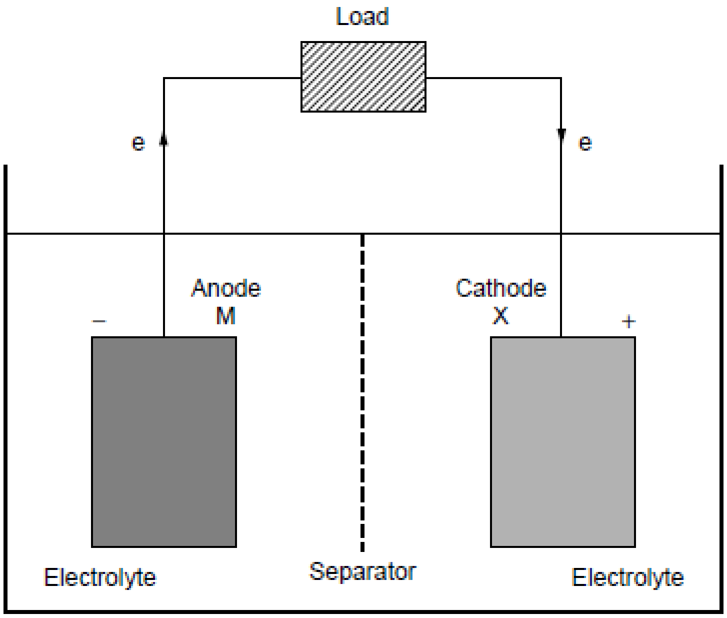

Figure 1.1 General schematic of an electrochemical cell showing electron movement upon discharge.[10]

Charging requires the input of energy to move lithium ions up their electrochemical potential gradients. Upon discharge, lithium ions migrate back to the cathode from the anode through the electrolyte while electrons flow through the external circuit toward the cathode. During this spontaneous process, the current generated in the external circuit powers an external load.

In order to optimize a lithium-ion battery for a given situation, several thermodynamic factors must be accounted for – these are summarized in Figure 1.2. The open-circuit potential (V_{oc}) of a lithium-ion battery depends on the choice of both the cathode and anode materials. The potential may be maximized by selecting an anode material with a small work function (ϕ_a) and a cathode material with a large work function (ϕ_c) according to the relationship:

$$V_{oc} = \frac{\phi_c - \phi_a}{e} \tag{1.1}$$

The choice of electrolyte, however, places limits on the energies of the cathode and anode. The Fermi energies of each must be within the band gap (E_g) of the electrolyte. If the Fermi energy of the cathode is lower than the highest occupied molecular orbital (HOMO) of the electrolyte, then the electrolyte will be oxidized. Similarly, the electrolyte will be reduced if the Fermi energy of the anode is higher than the lowest unoccupied molecular orbital (LUMO) of the electrolyte.

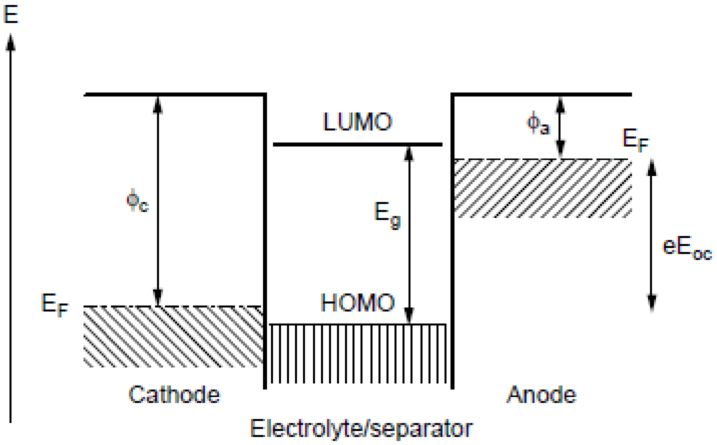

Figure 1.2 Energy diagram of an electrochemical cell at open circuit.[10]

With these considerations in mind, a number of requirements must be met to achieve satisfactory performance. As previously stated, the potential difference between the cathode and the anode should be high while remaining within the band gap of the electrolyte in order to maximize the operating voltage (and capacity). In addition, the electrolyte should have high lithium-ion conductivity but low electronic conductivity. The separator should also mitigate chances of a short circuit. Furthermore, both the cathode and the anode should be structurally stable upon cycling to mitigate capacity loss. They should also possess high lithium-ion and electronic conductivity to improve the charge-discharge rate capability. Finally, all materials used in the battery should be relatively inexpensive and environmentally friendly.

While the open-circuit voltage of a lithium-ion battery can be calculated using thermodynamic considerations (Eq. 1.1), the actual voltages observed during cycling (known as the operating voltage, V_{op}) also depend on polarization losses. The net effect of polarization losses is thermal energy waste. There are three classifications of polarization loss: activation polarization (η_a), concentration polarization (η_c), and ohmic polarization (IR). Activation polarization depends on the electrode reaction kinetics. Concentration polarization is caused by concentration differences of the products and reactants near the electrodes vs the bulk solution due to finite mass transfer kinetics. Ohmic polarization, also known as IR drop, is simply the internal resistance of the cell. This includes both electronic resistance of the electrodes and ionic resistance of the electrolyte. Added together, these polarization losses relate the open circuit voltage to the operating voltage:

$$V_{op} = V_{oc} - (\eta_a + \eta_c + IR) \tag{1.2}$$

It should be noted that the overall polarization loss of a cell is proportional to the current. Thus, the open-circuit voltage will only be approximated by the operating voltage at very low currents. As these polarization losses are clearly material-dependent, a judicious choice of cathode and anode materials will allow faster charge and discharge while maintaining a reasonable voltage.

Total cell capacity is limited by the electrode with the lower capacity. Since the widely used graphite anode has a significantly higher specific capacity than the currently utilized cathode materials (372 Ah kg^{-1} vs < 200 Ah kg^{-1}), it is imperative to discover and optimize new cathode materials in order to improve overall capacity and energy density.

1.2.2 Layered Oxide Cathodes

As previously mentioned, layered oxide cathodes with the general formula $LiMO_2$ (M = V, Cr, Co, and Ni) were the first to be explored among oxides. Specifically, $LiCoO_2$ was the first cathode material used by Sony in 1991.[7] Even today, most lithium-ion batteries use $LiCoO_2$. These materials crystallize in the α-$NaFeO_2$ structure (Figure 1.3).

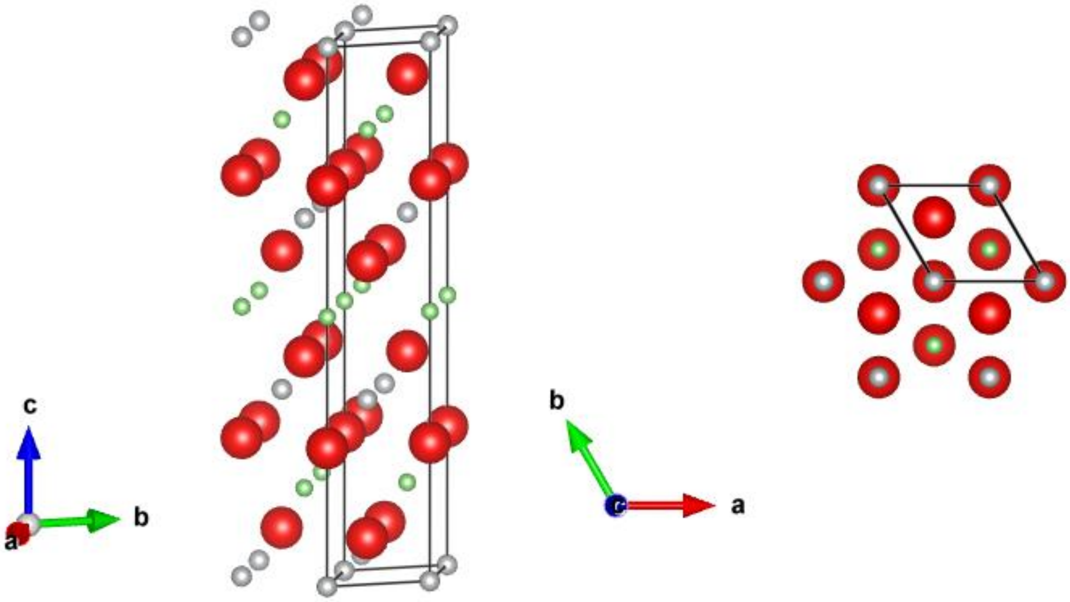

Figure 1.3 Crystal structure of layered $LiMO_2$.[13]

In this structure, O^{2-} ions form a cubic close-packed array. Li^+ and M^{3+} ions occupy the octahedral interstitial sites on alternating (111) planes of the rock salt structure. This gives an alternating sequence of Li-O-M-O-Li-O-M-O-Li… along the *c* axis of the unit cell in Figure 1.3. In Delmas notation,[14] this is known as the O3 structure because the metal ions occupy the octahedral sites and three MO_2 layers are present per unit cell. This layered structure allows fast two-dimensional Li^+ diffusion, assuming there is no cation disorder. The edge-shared MO_6 octahedra provide direct M-M orbital overlap, enabling excellent electronic conductivity.

The utility of $LiCoO_2$ over other materials in the layered oxide family is a result of several factors. First, it is easy to synthesize. Heating stoichiometric amounts of intimately mixed LiOH and Co_3O_4 powders in air at 800 ^{o}C produces a phase-pure sample with excellent electrochemical properties. The active $Co^{3+/4+}$ redox couple provides a stable operating voltage of approximately 4 V vs Li/Li^+. In addition, low-spin Co^{3+} and Co^{4+} have a strong octahedral site preference, reducing migration of these ions to the lithium plane via tetrahedral sites.

Unfortunately, $LiCoO_2$ also suffers from several drawbacks. Most importantly, the practical capacity of $LiCoO_2$ (~ 140 Ah kg^{-1}) is only half the theoretical capacity. That is, only half of the Li^+ can be reversibly extracted due to irreversible phase transformations and oxygen loss at lower Li^+ contents.[15,16] Additionally, cobalt is a relatively expensive and toxic metal with a high environmental impact upon disposal.

$LiNiO_2$ also crystallizes in the O3 structure. The $Ni^{3+/4+}$ redox couple is similar in energy to that of cobalt, resulting in similar charge/discharge voltages. While nickel is less expensive and more environmentally benign than cobalt, stoichiometric $LiNiO_2$ is difficult to synthesize[17] and it suffers from rapid capacity fade on cycling.[18] Due to the stability of Ni^{2+}, synthesized $LiNiO_2$ often has the composition $[Li_{1-x}Ni_x]_{3a}[Ni_{1-x}]_{3b}[O_2]_{6c}$ where Ni^{2+} sits in a Li^+ site. This cation disordering drastically reduces electrochemical performance by reducing Li^+ diffusion. Even with a near-stoichiometric synthesis, nickel ions will migrate to the lithium plane upon cycling.

1.2.3 Spinel Oxide Cathodes

The cubic spinel $LiMn_2O_4$ and its derivatives have been studied extensively as attractive cathode materials.[19,20] Manganese is an attractive choice because it is not environmentally harmful and it is inexpensive. In addition, the cubic spinel crystal structure maintains its integrity upon cycling and allows for rapid, 3-dimensional Li^+ diffusion. This is evident upon examination of its crystal structure (Figure 1.4).

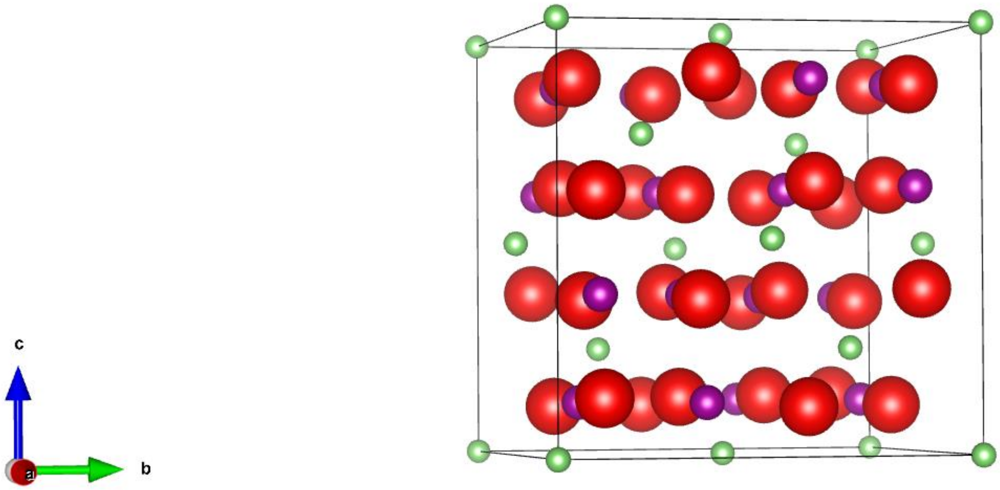

Figure 1.4 Crystal structure of $LiMn_2O_4$ spinel.[13]

$LiMn_2O_4$ crystalizes in the cubic space group *Fd-3m*. Like the layered structure, the spinel structure has a close-packed oxygen array. The O^{2-} ions occupy the 32e Wyckoff positions. $Mn^{3+/4+}$ ions occupy alternate octahedral interstitial sites (16d), while Li^+ ions occupy ordered tetrahedral interstitial sites (8a) along the unit cell's body diagonal. A shorthand notation to specify this structure is $(Li)_{8a}[Mn_2]_{16d}O_4$. Since half of the octahedral sites (16c) are vacant, it is possible to insert a second equivalent of Li^+ ions to form $Li_2Mn_2O_4$. The addition of a second Li^+, however, causes two structural changes. First, the Li^+ ions in the lattice move from 8a tetrahedral sites to 16c octahedral sites to alleviate electrostatic repulsion. This forms the ordered rock salt phase $\{Li_2\}_{16c}[Mn_2]_{16d}O_4$. Second, incorporation of extra Li^+ reduces the Mn^{4+} ions to Mn^{3+} to maintain charge neutrality. The Mn^{3+} ion undergoes a Jahn-Teller distortion. Due to its single e_g electron, high spin Mn^{3+} ($t_{2g}^3e_g^1$) experiences a tetragonal distortion to reduce its overall energy. When sufficient Mn^{4+} has been reduced to Mn^{3+}, a cubic to tetragonal phase transition occurs, resulting in an abrupt 6.5 percent increase in unit cell volume. This substantial, abrupt volumetric expansion leads to fast capacity fade upon cycling due to electrode damage.

Li^+ insertion into 8a tetrahedral sites occurs around 4 V, while Li^+ insertion into 16d octahedral sites occurs around 3 V. Thus, one would expect capacity fade due to Jahn-Teller distortion to be mitigated by cycling only in the 4 V region. Unfortunately, capacity fade still occurs due to several factors. Several strategies have been employed to circumvent the capacity fade of $LiMn_2O_4$ – most notably substation of Mn with both redox active[21,22] and redox inactive[23,24] metal ions. Substitution with extra Li to form $(Li)[Mn_{1.67}Li_{0.33}]O_4$ completely removes the 4 V plateau. In contrast, substitution with a 3d transition metal (M = Cr, Fe, Co, and Ni) to form $(Li)[Mn_{2-x}M_x]O_4$ results in two distinct plateaus corresponding to Li^+ insertion into the 8a tetrahedral sites. The expected 4 V plateau corresponds to the $Mn^{3+/4+}$ redox couple, while the new 5 V plateau corresponds to the $M^{3+/4+}$ redox couple. These compounds are known as high-voltage spinels.

1.2.4 Layered-to-Spinel Transition

The transition from the O3 layered to the spinel structure for several $Li_{0.5}MO_2$ (M = V, Co, and Ni) compositions has been studied at length.[25-39] This process first requires removal of half of lithium ions from the parent $LiMO_2$. This can be done by either chemical delithiation or electrochemical charging. However, it is difficult to chemically characterize the electrochemically delithiated samples due to the presence of conductive carbon and binder in the electrodes. Chemical delithiation also has the added advantages of fast reaction time (typically 1 – 48 h) and scalability. The choice of chemical oxidant depends on the reduction potential of the transition metal ion, but several oxidants have been used. These include, in order of increasing reduction potential vs Lithium, Br_2, $Na_2S_2O_8$, and NO_2BF_4 (or NO_2PF_6). For NO_2BF_4, the overall Li^+ extraction reaction can be summarized as:

$$LiMO_2 + xNO_2BF_4 \rightarrow Li_{1-x}MO_2 + xNO_2 + xLiBF_4 \qquad (1.3)$$

While Br_2 and $Na_2S_2O_8$ are relatively air stable, NO_2BF_4 violently decomposes in air and must be handled in air-free and water-free conditions. Once a stoichiometry near $Li_{0.5}MO_2$ is achieved, thermally induced cation migrations must take place within the close-packed oxygen lattice to afford the spinel phase. Specifically, transformation to the spinel phase $(Li)_{8a}[M_2]_{16d}O_4$ necessitates a migration of ¼ of the transition metal ions $M^{3.5+}$ from the 3b octahedral sites of the M planes to the 3a octahedral sites of the Li planes. Additionally, all of the Li^+ ions must move from the 3a octahedral sites to the adjacent tetrahedral sites.[26]

The transition-metal ions must migrate between octahedral sites via tetrahedral sites, as shown in Figure 1.5.[26] In this illustration, M^{n+} ions must travel through tetrahedral sites T_1 and T_2 in order to fill vacant octahedral sites in the Li plane. With this requirement in mind, one can understand the 3d metal-dependent ease with which spinel transformation takes place by considering crystal field stabilization energies (CFSEs) of the ions of interest (Table 1.1).

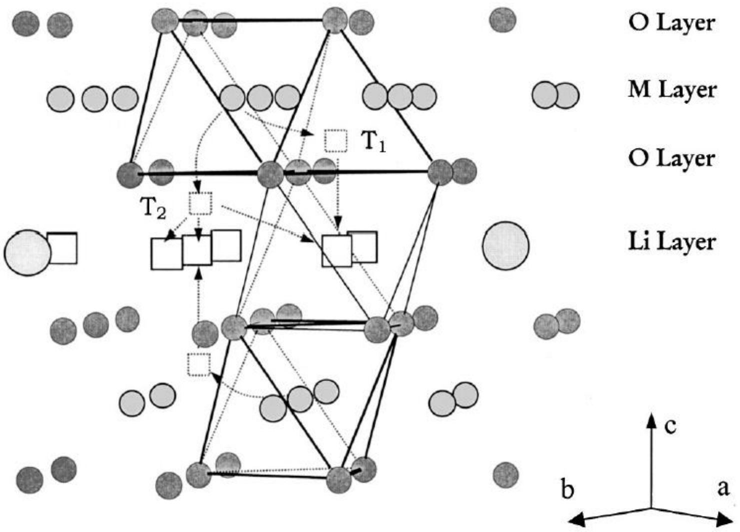

Figure 1.5 Schematic illustration of the movement of M^{n+} from the M layer to the Li layer via neighboring tetrahedral sites (T_1 and T_2).[25]

Table 1.1 CFSEs and OSSEs of selected 3d transition metal ions.[9,26]

Ion	***Octahedral Coordination***		***Tetrahedral Coordination***		
	Configuration[a]	**CFSE**	**Configuration**	**CFSE**[b]	**OSSE**[c]
Co^{3+}	$t_{2g}^6 e_g^0$ (LS)	-24 Dq	$e^3 t_2^3$ (HS)	-2.67 Dq	-21.33 Dq
Co^{4+}	$t_{2g}^5 e_g^0$ (LS)	-20 Dq	$e^2 t_2^3$ (HS)	0 Dq	-20.00 Dq
Ni^{3+}	$t_{2g}^6 e_g^1$ (LS)	-18 Dq	$e^4 t_2^3$ (HS)	-5.33 Dq	-12.67 Dq
Ni^{4+}	$t_{2g}^6 e_g^0$ (LS)	-24 Dq	$e^3 t_2^3$ (HS)	-2.67 Dq	-21.33 Dq
Cr^{3+}	$t_{2g}^3 e_g^0$ (LS)	-12 Dq	$e^2 t_2^1$ (HS)	-3.56 Dq	-8.44 Dq
Mn^{3+}	$t_{2g}^3 e_g^1$ (HS)	-6 Dq	$e^2 t_2^2$ (HS)	-1.78 Dq	-4.22 Dq
Mn^{4+}	$t_{2g}^3 e_g^0$ (HS)	-12 Dq	$e^2 t_2^1$ (HS)	-3.56 Dq	-8.44 Dq
V^{3+}	$t_{2g}^2 e_g^0$ (LS)	-8 Dq	$e^2 t_2^0$ (LS)	-5.33 Dq	-2.67 Dq
Fe^{3+}	$t_{2g}^3 e_g^2$ (HS)	0 Dq	$e^2 t_2^3$ (HS)	0 Dq	0 Dq

[a] LS and HS refer, respectively, to low-spin and high-spin electron configurations.

[b] Obtained by assuming that $\Delta_t = 4/9\Delta_o$; Δ_t and Δ_o refer, respectively, to tetrahedral and octahedral splittings.

[c] $OSSE = CFSE_{oct} - CFSE_{tet}$.

Crystal field stabilization energy quantifies the stability imparted on an ion when it enters a specified crystal-field geometry. In this case, only octahedral and tetrahedral geometries are of interest. For the ions of interest, the CFSE in octahedral coordination is larger or equal in magnitude than the CFSE in tetrahedral coordination. This preference for octahedral coordination, known as octahedral-site-stabilization energy (OSSE) is simply the difference between the two CFSEs. Note that all the values are negative or zero. This indicates a reduction in energy. The magnitude of the OSSE is a measure of the extent to which an ion prefers octahedral sites to tetrahedral sites in a crystal. Referring to Table 1.1, Co^{3+} and Co^{4+} have relatively high OSSEs. As a result, layered $Li_{0.5}CoO_2$ does not readily transform into a spinel structure upon prolonged heating.[26-28] In fact, $Li_{0.5}CoO_2$ tends to disproportionate below 400 °C to form a Co_3O_4 impurity and $LiCoO_2$ rather than transforming to spinel $LiCo_2O_4$.

Since Ni^{3+} has a significantly lower OSSE, layered $Li_{0.5}NiO_2$ transforms to a cubic spinel-like phase at 200 °C.[26,29-32] Unfortunately, Ni ions occupy both the 16c and 16d octahedral sites, indicating incomplete Ni migration. Heating to temperatures above 200 °C results in oxygen loss and the appearance of a nickel(II) oxide impurity. Layered $Li_{0.5}VO_2$ has been reported to slowly transform to a cubic spinel phase at room temperature – not surprisingly due to the low OSSE of V^{3+}.[34-37] Both monoclinic and orthorhombic $LiMnO_2$ form spinel-like phases upon delithiation at ambient temperatures without heating. Again, this would be expected based on the low OSSEs of $Mn^{3+/4+}$.

Finally, it should be noted that there is a thermodynamic driving force for the layered-to-spinel phase transition – first principles calculations have verified the lower energy of the spinel structure for all 3d metals discussed.[38]

1.3 OXYGEN EVOLUTION CATALYSIS

As alluded to in Section 1.1, both metal-air batteries including lithium-air batteries and photoelectrochemical water splitting for H_2 generation are currently highly active areas of research. Although they have significantly more challenges than lithium-ion batteries, they may one day enable the generation and storage of energy at a significantly higher density and/or lower cost than current lithium-ion batteries. Both of these technologies require highly active catalysts for the oxygen evolution reaction (OER).

1.3.1 Purpose

Lithium-air batteries[40] use the oxidation of lithium metal at the anode and the reduction of oxygen at the cathode to produce electricity. During charging, however, lithium is plated back onto the anode and oxygen is regenerated from O^{-2} at the cathode. Although they have extremely high theoretical energy density (11,140 Wh/kg of Li), they are marred by many daunting issues. One of the most prominent issues is the poor oxygen redox kinetics at the cathode. Thus, an improved OER catalyst is essential.

Photoelectrochemical (PEC) water splitting is a process that converts abundant solar energy into chemical energy in the form of hydrogen.[41,42] Hydrogen can then be stored and used when energy demands rise. In PEC water splitting, H_2O is converted into H_2 and O_2. This typically requires the use of two separate catalysts – an OER catalyst and a hydrogen evolution reaction (HER) catalyst. At present, the OER is significantly less efficient than the HER. As a result, an improved OER catalyst would make PEC water splitting accessible.

1.3.2 Operating Principles

The electrochemical evolution of O_2 from water at the anode of an electrochemical cell may be written as:

$$2H_2O\ (l) \rightarrow O_2 + 4H^+ + 4e^- \quad E^o = 1.23\ \text{V vs. SHE} \tag{1.4}$$

where SHE is the standard hydrogen electrode. One accepted general mechanism[43] (Equations 1.5-1.8) begins with water adsorption and dissociation on the metal oxide catalyst to form OH_{ads}. The OH_{ads} is oxidized to O_{ads}, and a second water molecule reacts to form a superoxide intermediate (OOH_{ads}). Finally, a fourth oxidation results in O_2 evolution.

$$H_2O \rightleftharpoons OH_{ads} + H^+ + e^- \tag{1.5}$$

$$OH_{ads} \rightleftharpoons O_{ads} + H^+ + e^- \tag{1.6}$$

$$H_2O + O_{ads} \rightleftharpoons OOH_{ads} + H^+ + e^- \tag{1.7}$$

$$OOH_{ads} \rightleftharpoons O_2 + H^+ + e^- \tag{1.8}$$

The primary issue with the OER is the large overpotential that must be supplied at the anode. This translates into significant energy loss.[44] The origin of this large thermodynamic overpotential requirement is the sequential four-electron oxidation. Specifically, a catalyst must serve as a host for three different intermediates with different binding energies. Another method to reduce the potential of the OER is to run the reaction in alkaline medium.[45] This increases the concentration of available OH^-.

A number of catalysts have been developed to lower the activation energy of this reaction. Catalysts are typically transition-metal oxides. Since oxygen evolution on metal electrodes occurs at potentials above 0.401 V vs. SHE in alkaline electrolyte, metal catalysts will possess an oxide layer on their surface.[43] Currently, the perovskite

$Ba_{0.5}Sr_{0.5}Co_{0.8}Fe_{0.2}O_{3-\delta}$ (BSCF) shows the highest catalytic activity, followed by RuO_2, IrO_2, $NiCo_2O_4$, and $LaNiO_3$.[46] Generally, oxides of Co, Ni, and Fe exhibit significant electrocatalytic activities. Recently, spinels containing these transition metals have been investigated for OER.[47,48] These materials are attractive OER catalyst candidates due to their relatively low cost, ease of synthesis, high electronic conductivity, and stability in basic solution.

1.4 THESIS OBJECTIVES

Chemical extraction of Li^+ from a metal oxide is well precedented. This soft chemistry method may be used to synthesize metastable phases at or near room temperature. In addition, moderate temperature heating of these metastable phases may afford new phases that are inaccessible by direct high-temperature synthesis. Accordingly, the primary objectives of this thesis are to prepare Fe- and Mn-substituted layered $LiNiO_2$ materials, perform chemical delithiation on them to afford metastable phases, and anneal the delithiated materials in order to transform them to a cubic spinel phase. These materials, several of them unknown in the literature, are characterized by inductively coupled plasma optical emission spectroscopy (ICP-OES) and x-ray diffraction (XRD). Furthermore, their electrochemical properties and OER catalytic properties are explored.

Chapter 2: Experimental Methods

2.1 MATERIALS SYNTHESIS

2.1.1 Synthesis of Layered Oxides from Nitrate Precursors

Layered $LiNi_{1-x-y}Mn_xFe_yO_2$ oxides were synthesized from nitrate precursors according to the method of Guo and Greenbaum.[49] First, a proper stoichiometric quantity of $LiOH\cdot H_2O$ was dissolved in deionized water (200 mL) in a 1 L beaker. Then concentrated HNO_3 was added to $pH < 2$ using pH papers. This process produced a highly pure solution of $LiNO_3$ from the readily weighed $LiOH\cdot H_2O$. Proper stoichiometric amounts of hydrated transition-metal nitrates ($Ni(NO_3)_2\cdot 6H_2O$, $Mn(NO_3)_2\cdot 4H_2O$, $Fe(NO_3)_3\cdot 9H_2O$) were then added to form a clear solution. This solution was stirred and heated to 200 ^{o}C for several hours in order to evaporate the water, resulting in a viscous mixed-metal nitrate mixture. Stirring was discontinued, and the mixed-metal nitrates dehydrated and partially decomposed as evidenced by the evolution of a yellow gas. The resulting black solid was ground in an agate mortar into a fine powder. It should be noted that heating well above 200 ^{o}C results in further decomposition and a material that is very hygroscopic and difficult to grind. The powder was fired twice in a tube furnace under O_2 atmosphere for 6 hours with intermediate grinding to afford the layered compound as a black powder. For all materials, the calcination temperature was 700 ^{o}C. For $LiNi_{0.6}Mn_{0.3}Fe_{0.1}O_2$, a third calcination at 850 ^{o}C under flowing O_2 for 6 hours was necessary to achieve phase purity. Samples were stored in a vacuum desiccator until further use.

2.1.2 Chemical Delithiation

The layered oxide powders were combined with solid NO_2BF_4 (Matrix Scientific, 0.5-3 equivalents) in an oven-dried round bottom flask within an argon-filled glovebox. The flask was fitted with a rubber septum and transferred to a Schlenk line. Dry acetonitrile was added via syringe, and the reaction was stirred under argon at room temperature for 48 hours. The reaction was diluted with wet acetonitrile, and the powder was collected via vacuum filtration with a fine fritted funnel. The powders were washed with acetonitrile until the filtrate was clear. The powders were transferred to glass vials and dried in an oven at 100 ^{o}C for several hours. The vials were stored in a vacuum desiccator until further use.

2.1.3 Low-Temperature Annealing

Often, the lithium in the layered compounds was slightly overextracted (under 0.5 stoichiometry). Thus, a mixture of the as-prepared layered compound and the delithiated compound was ground in an agate mortar in order to achieve a stoichiometry of $Li_{0.5}MO_2$. These powders were annealed in an oven at temperatures ranging from 200-450 ^{o}C for 5-7 days. The spinel-like products were stored in a vacuum desiccator until further use.

2.2 POWDER X-RAY DIFFRACTION

In x-ray diffraction (XRD), an incident x-ray beam is scattered by a crystal according to Bragg's law of diffraction:

$$n\lambda = 2d\sin\theta \qquad (2.1)$$

where n is an integer, λ is the wavelength of incident radiation, d is the interplanar spacing, and θ is the angle between the incident radiation and the plane normal. In XRD, n is typically chosen to be 1. Since this scattering depends intimately on the crystal structure of the material, an XRD pattern is specific to the crystal structure. Thus, XRD patterns may be used for phase identification. In addition, an analysis of the XRD pattern, known as Rietveld refinement, may be used to determine lattice parameters, nonstoichiometry, and cation disorder. In a powder XRD experiment, a flat powder sample is irradiated with x-rays over a range of angles (θ). Since the incident and reflected beams are at the same angle to the sample, a detector is placed at 2θ to measure intensity. This intensity is then plotted vs 2θ in an XRD pattern.

Powder x-ray diffraction patterns were collected with a Rigaku Ultima-IV diffractometer with Cu Kα radiation. Patterns were recorded over a 2θ range of $10 – 80^o$ with a step size of 0.02^o and a dwell time of 4 s per step. Rietveld refinement was performed using the Fullprof software suite.[50] Lattice parameters of unrefined patterns were obtained manually with a Q-chart on Microsoft Excel. The d-spacings of the cubic patterns were obtained from the PDXL software package.[51]

2.3 INDUCTIVELY COUPLED PLASMA OPTICAL EMISSION SPECTROSCOPY (ICP-OES)

Inductively coupled plasma optical emission spectroscopy (ICP-OES) is a widely used analytical technique to determine molar ratios of metallic elements.[52] In an ICP-OES experiment, a sample is acid-digested and aerosolized by a nebulizer. The aerosol is directed toward an inductively coupled plasma that is at a temperature of approximately 10,000 K. At this temperature, analytes enter the gas phase and are promoted to excited states. When these excited species relax to their ground state, they emit photons at characteristic wavelengths. As different elements have unique emission spectra, the wavelengths of light emitted can be used to identify the elements present. In addition, the amount of each element present can be determined based on the intensities of the emitted light.

A Varian 715-ES inductively coupled plasma optical emission spectrometer was used to determine the Li, Ni, Mn, and Fe molar ratios in the layered and delithiated materials. Approximately 3 mg of each of the samples was dissolved in concentrated acid (1.5 mL HCl and 0.5 mL HNO_3) with heating. After complete dissolution, the solutions were diluted with deionized water so that the concentrations of the metal ions were all within the concentration range of the prepared standard solutions. The spectrometer was calibrated with a blank solution and three standard solutions containing all the ions of interest. All samples were analyzed in triplicate.

2.4 ELECTROCHEMICAL CHARACTERIZATION

2.4.1 Electrode Preparation

Cathode slurries were prepared by combining 80 wt. % active material, 10 wt. % polyvinylidene fluoride (PVDF) binder, and 10 wt. % Super P conductive carbon in a scintillation vial. Enough N-methyl-2-pyrrolidone (NMP) was added to achieve a paint-like consistency, and the slurries were stirred overnight. The slurries were cast onto aluminum foil, dried at 100 ^{o}C in an oven, and stored in a vacuum oven at 100 ^{o}C until further use.

2.4.2 Cell Assembly & Galvanostatic Testing

Cathodes were punched out and combined with lithium as the anode in CR2032 coin cells. Coin cells were assembled in a glove box under argon atmosphere. Celgard polypropylene was used as a separator, and the electrolyte was 1 M $LiPF_6$ in 1:1 ethylene carbonate (EC):diethyl carbonate (DEC). Constructed batteries were allowed to rest a minimum of six hours before testing. An Arbin battery cycler was used for all electrochemical tests. All galvanostatic tests were performed at a rate of C/10. Layered cathodes were cycled from 3 to 4.5 V vs. Li, and spinel-like cathodes were cycled from 3 to 4.9 V vs. Li. Specific capacities were calculated based on the mass of active material in each cell.

2.5 OXYGEN EVOLUTION CATALYSIS

2.5.1 Catalyst Ink Preparation

Catalyst inks were prepared by combining 25 mg of active oxide material, 5 mg of acetylene black, 154 μL of Liquion solution containing 0.1 M NaOH (2:1 v/v), and 5 mL of ethanol in a tall scintillation vial. Liquion is a proprietary blend of nafion conductive polymer in a mixture of alcohols. The inks were sonicated for 30 minutes and aged overnight before use.

2.5.2 Oxygen Evolution Reaction Experiments

All oxygen evolution reaction experiments were performed with a three-electrode cell connected to an Autolab PGSTAT302N potentiostat (Figure 2.1). The working electrode was prepared by depositing 5 μL of a catalyst ink (0.025 mg of active material) onto a glassy carbon electrode with an area of 0.196 cm^2 encased in Teflon and allowing the ink to slowly air dry under an upside down beaker. This slow drying process allows the catalyst to be deposited evenly on the surface of the electrode. Before each ink deposition, the glassy carbon electrode was polished with 0.05 μm alumina paste and rinsed with deionized water to ensure a smooth surface. All potentials are reported vs. the saturated calomel electrode (SCE), which was used as the reference electrode. The working electrode was rotated at a constant 1600 rpm, and the counter electrode was platinum mesh separated by a porous glass frit.

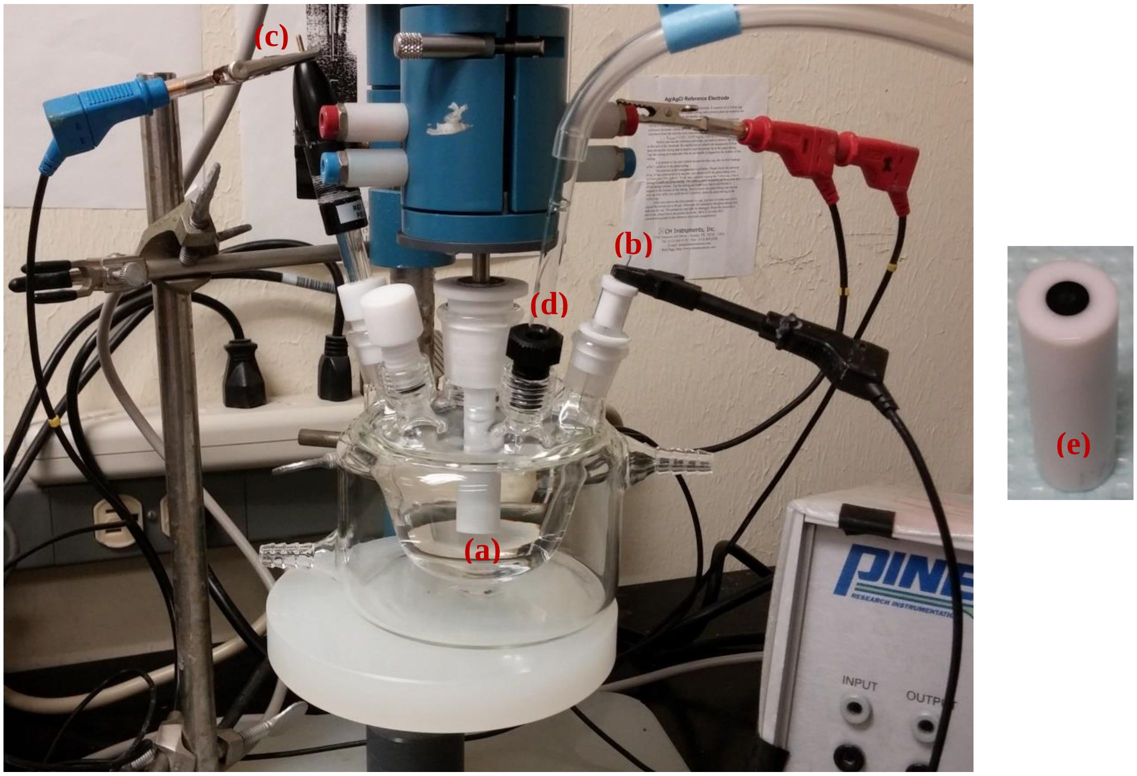

Figure 2.1 OER experimental setup with (a) the rotating glassy carbon (working) electrode, (b) the platinum (counter) electrode, (c) the SCE (reference) electrode, and (d) the O_2 infusion line, and (e) a close-up of the glassy carbon electrode.

Cyclic voltammetry (CV) is an electrochemical technique where the potential is swept at a constant rate to a set potential and then swept back at the same rate. For all OER experiments, the electrolyte consisted of a 0.1 M KOH solution in deionized water that was saturated with high purity O_2 by constantly bubbling it in from a tank. CV scans were recorded from 0 to 1 V vs. SCE at a rate of 10 mV/s. All experiments were performed at room temperature.

2.5.3 Surface Area Measurements

Specific surface area of selected metal oxide powders was determined with a Brunauer-Emmett-Teller (BET) surface area analyzer (NOVA 2000, Quantachrome).

Chapter 3: Results and Discussion

3.1 STRUCTURAL CHARACTERIZATION & ELEMENTAL ANALYSIS

XRD patterns of the materials synthesized in this study are shown in Figures 3.1 and 3.2. In each grouping, the bottom pattern is the 'as-prepared' $LiMO_2$ layered sample, while the pattern directly above is the delithiated sample. Patterns above the bottom two are delithiated phases that have been annealed at various temperatures. Both 'as prepared' and delithiated samples clearly possess the layered O3 structure, as indicated by the separation of the (018) and (110) reflections around $2\theta = 65^o$.

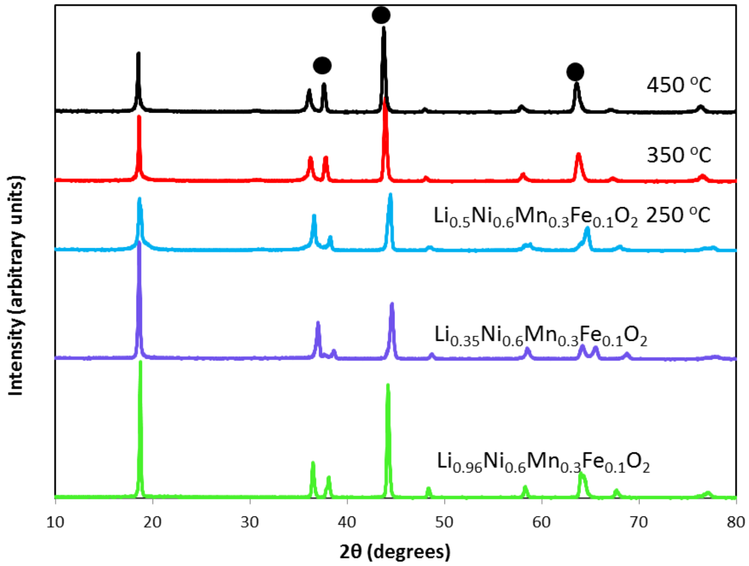

Figure 3.1 XRD patterns of the '$LiNi_{0.6}Mn_{0.3}Fe_{0.1}O_2$' series of compounds. The symbol ● corresponds to a NiO impurity phase.

ICP-OES analysis of the 'as-prepared' layered materials indicates a lithium stoichiometry below unity in all cases. This is to be expected, as $LiNiO_2$ always has non-stoichiometry due to the tendency of Ni^{3+} to be reduced to Ni^{2+} under the high-temperature synthesis conditions. As Ni^{2+} is much closer in size to Li^{+} than Ni^{3+} is, Ni^{2+} populates the lithium layer. This leads to the formula $Li_{1-x}Ni_{1+x}O_2$.[53] Upon Fe substitution, this effect becomes even more pronounced.

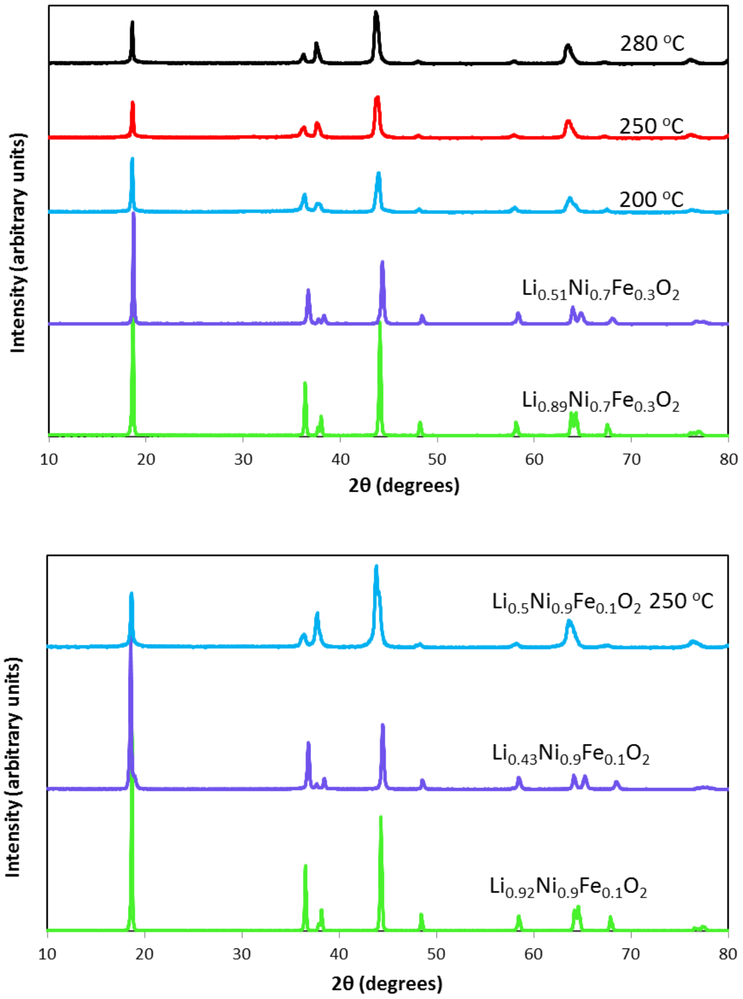

Figure 3.2 XRD patterns of the '$LiNi_{0.7}Fe_{0.3}O_2$' and '$LiNi_{0.9}Fe_{0.1}O_2$' series of compounds.

Rietveld refinement of the layered compounds was performed with the Fullprof software in a manner similar to Prado and Delmas.[53] Refinement was first done assuming a perfect layered structure with *R-3m* space group and unit lithium stoichiometry (Li = Ni + Fe). In this structure, lithium occupies the 3b Wyckoff position (0,0,1/2) and the transition metals occupy the 3a Wyckoff position (0,0,0). Oxygen occupies the 6c Wyckoff position (0,0,z), where z is approximately 1/4 but can be refined. The lattice parameters, scale factor, full width at half maximum (FWHM) parameters, shape parameters, background, sample height correction, and oxygen z-coordinate were refined first. Then, the occupancies of the lithium and nickel in the 3b position were allowed to vary with the constraint that they add to one. Due to difficulties in refining the isotropic atomic displacement parameters, they were fixed to their ideal values in $LiNi_{0.7}Co_{0.3}O_2$ [B(Li) = 1.0 $Å^2$, B(3d metal) = 0.5 $Å^2$, B(O) = 0.8 $Å^2$]. Thermal parameters may be difficult to refine in XRD patterns, and are much easier in neutron diffraction patterns.[54] This procedure assumes that only Li^+ and Ni^{2+} occupy the 3b sites and does not account for Ni^{3+} or Fe^{3+} in the lithium layer. A summary of the refinement process is shown in Table 3.1.

It is interesting to note the comparison in the Li composition from ICP-OES and XRD data refinement for the two layered materials containing only Ni and Fe. For $Li_{1-x}Ni_{0.7}Fe_{0.3}O_2$, ICP-OES and refinement provided a Li : 3d metal ratio of, respectively, 0.89 and 0.83. For $Li_{1-x}Ni_{0.9}Fe_{0.1}O_2$, ICP-OES and refinement provided a Li : 3d metal ratio of, respectively, 0.92 and 0.93. Although ICP-OES compositions should be regarded as more accurate than refinement data, this close agreement suggests that the assumption of only Ni^{2+} in the lithium plane is reasonable. In contrast, ICP-OES and refinement provided a Li : 3d metal ratio of, respectively, 0.96 and 0.75 for $Li_{1-x}Ni_{0.6}Mn_{0.3}Fe_{0.1}O_2$.

This discrepancy strongly suggests that, in addition to Ni^{2+}, other 3d metal ions could also populate the lithium layer.

Table 3.1 Lattice parameters and Rietveld refinement data for layered compounds and their corresponding delithiated compounds.

Sample[a]	**a (Å)**	**c (Å)**	$\mathbf{z_{ox}}$[b]	**z**[c]	$\mathbf{R_B}$	χ^2
$Li_{0.89}Ni_{0.7}Fe_{0.3}O_2$	2.9019	14.3478	0.2566	0.0945	4.678	0.515
$Li_{0.51}Ni_{0.7}Fe_{0.3}O_2$	2.8830	14.3700	0.2546	0.0871	12.95	0.720
$Li_{0.92}Ni_{0.9}Fe_{0.1}O_2$	2.8838	14.2491	0.2563	0.0357	3.438	0.936
$Li_{0.43}Ni_{0.9}Fe_{0.1}O_2$	2.8588	14.3288	0.2619	0.0219	6.827	1.130
$Li_{0.96}Ni_{0.6}Mn_{0.3}Fe_{0.1}O_2$	2.8970	14.3073	0.2566	0.1416	6.272	0.647
$Li_{0.35}Ni_{0.6}Mn_{0.3}Fe_{0.1}O_2$	2.8538	14.3548	0.2597	0.0820	13.93	0.846
[d]$Li_{0.76}Ni_{0.8}Fe_{0.2}O_2$	2.8979	14.3084	0.2571	0.1362	2.642	0.536
[d]$Li_{0.89}Ni_{0.95}Fe_{0.05}O_2$	2.8824	14.2317	0.2559	0.0578	3.171	0.845
[d]$Li_{0.49}NiO_2$	2.9005	14.2493	0.2562	0.3433	3.479	0.616

[a] Lithium stoichiometry was determined by ICP-OES.
[b] z_{ox} is the z-coordinate of the Wyckoff position of the oxygen ion in the structure.
[c] z is the amount of 3d metal in the lithium plane.
[d] Lithium stoichiometry was estimated from Rietveld refinement.

The XRD patterns of the delithiated samples were refined in a slightly different manner than those of the original samples. Refinement was first done assuming a perfect layered structure with *R-3m* space group and fixed lithium stoichiometry as determined by ICP-OES. The same parameters were refined as described above. Then, the occupancies of the 3d metals in the 3a and 3b sites were refined with the constraint that they add to unity. This was done because the presence of a large number of Li vacancies may allow the migration of 3d metal ions to the Li plane – especially Fe^{3+} due to its zero OSSE (see Table 1.1).

Referring to Table 3.1, the changes in the lattice parameters upon delithiation follow a common trend. For all samples, delithiation results in a decrease in **a** and an increase in **c**. This is verified by a previous report.[53] As more Li^+ is removed from the structure, more 3d ions are oxidized to their 4^+ state. This results in a contraction of the metal-oxygen bonds within the 3d layer and a decrease in **a**. The removal of Li^+ also increases the electrostatic repulsions between oxygen ions in adjacent layers, resulting in an increase in **c**.

As shown in Figures 3.1 and 3.2, heating the layered phases of composition $Li_{0.5}M_{0.5}O_2$ to moderate temperatures promotes a phase change to a cubic spinel-like phase. This is indicated by the coalescence of the (018) and (110) reflections to a single (440) reflection. For the $Li_{0.5}Ni_{0.6}Mn_{0.3}Fe_{0.1}O_2$ phase, extended heating at 250 °C results in a biphasic spinel-like material as indicated by the multiple peaks around $2\theta = 65^o$. Upon heating to 350 °C, the (440) reflection becomes more pronounced, but a NiO impurity appears due to oxygen loss. This NiO impurity is shown in Figure 3.1, where the indicated peaks have a significantly higher intensity than would be expected for pure spinel. In contrast, the $Li_{0.51}Ni_{0.7}Fe_{0.3}O_2$ and $Li_{0.5}Ni_{0.9}Fe_{0.1}O_2$ phases form a NiO impurity at the lower temperature of 250 °C. After a 200 °C thermal treatment, $Li_{0.51}Ni_{0.7}Fe_{0.3}O_2$ also forms a biphasic spinel-like material. These results indicate that temperatures required for complete spinel transformation are higher than temperatures at which oxygen loss occurs to form a NiO impurity under air atmosphere. The inability to access the ideal spinel $(Li)_{8a}[Ni_2]_{16d}O_4$ by heating $Li_{0.5}NiO_2$ under air atmosphere has been documented previously, as has the higher thermal stability of the rhombohedral $Li_{0.5}NiO_2$ phase upon substitution with Mn.[26]

3.2 ELECTROCHEMICAL PERFORMANCE

Galvanostatic charge/discharge curves for $Li_{0.89}Ni_{0.7}Fe_{0.3}O_2$ and $Li_{0.92}Ni_{0.9}Fe_{0.1}O_2$ are shown in Figure 3.3.

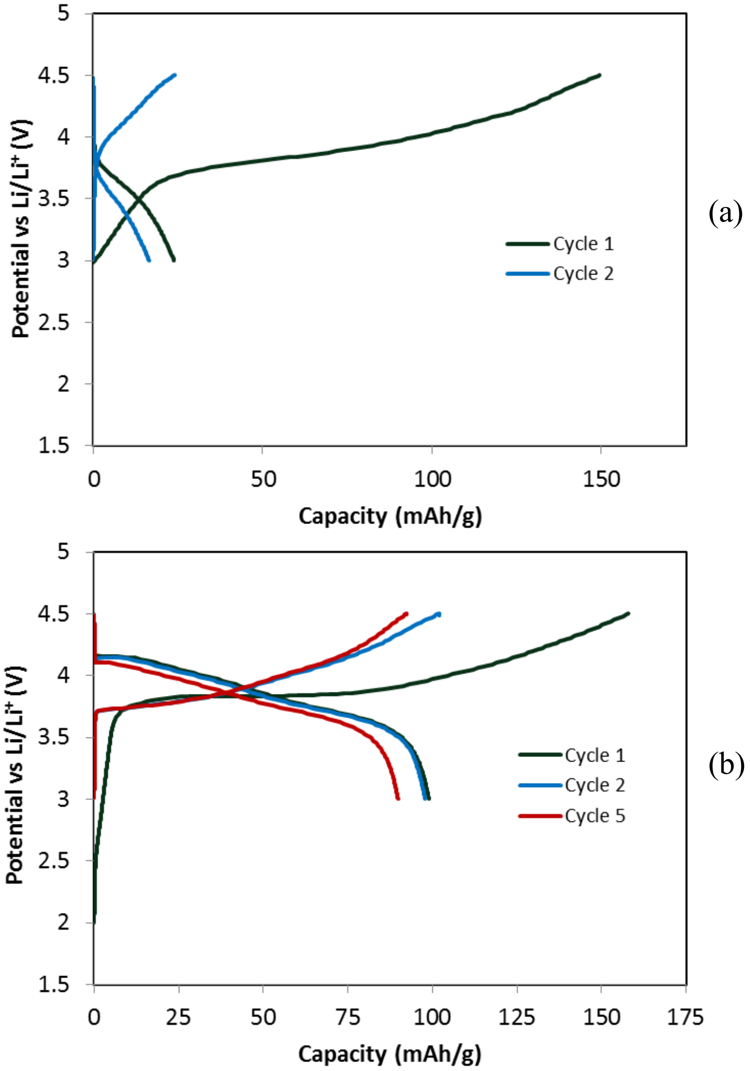

Figure 3.3 Charge/discharge curves of (a) $Li_{0.89}Ni_{0.7}Fe_{0.3}O_2$ and (b) $Li_{0.92}Ni_{0.9}Fe_{0.1}O_2$.

The difference in reversible capacities upon cycling between these two materials is substantial. While $Li_{0.92}Ni_{0.9}Fe_{0.1}O_2$ demonstrates an initial irreversible capacity loss of about 150 mAh/g after the first charge, it maintains its capacity rather well over the first five cycles. $Li_{0.89}Ni_{0.7}Fe_{0.3}O_2$, on the other hand, loses most of its capacity on the first charge. These results are consistent with previous studies on these materials, and they reinforce the assertion that Fe substitution in $LiNiO_2$ expands the lattice and enables more Ni^{2+} to migrate to the lithium layer.[53,55] This, in turn, drastically reduces the amount of Li that can be extracted/inserted.

Although $Li_{0.51}Ni_{0.7}Fe_{0.3}O_2$ and $Li_{0.5}Ni_{0.9}Fe_{0.1}O_2$ do form spinel-like phases on heating, these materials exhibit minimal capacities upon galvanostatic cycling. In addition, the $Li_{0.5}Ni_{0.6}Mn_{0.3}Fe_{0.1}O_2$ samples that were heated to 350 and 450 ^{o}C also show poor electrochemical properties. This is likely due to incomplete transformation to an ideal spinel phase as well as the presence of a large NiO impurity phase. The only spinel-like material that exhibits a non-trivial capacity is $Li_{0.5}Ni_{0.6}Mn_{0.3}Fe_{0.1}O_2$ that was heated to 250 ^{o}C (Figure 3.4).

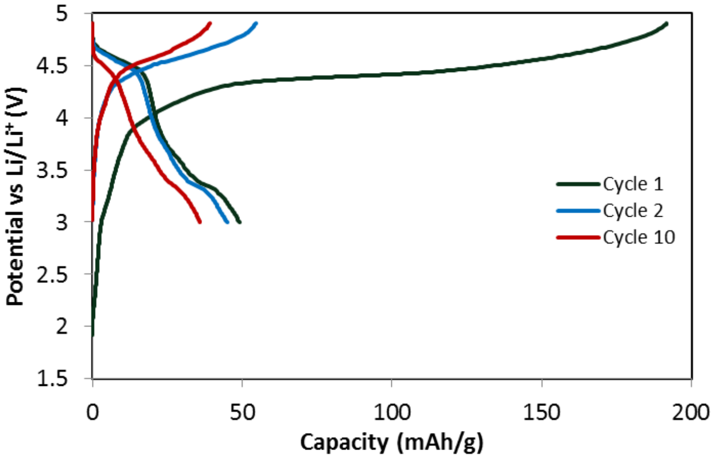

Figure 3.4 Charge/discharge curves of $Li_{0.5}Ni_{0.6}Mn_{0.3}Fe_{0.1}O_2$.

Although this material does show some reversible lithium deintercalation, it suffers a substantial capacity loss on initial charge. Moreover, the difference in charge plateau voltage on cycle 1 (~ 4.3 V) and cycle 2 (~ 4.6 V) suggests that a further phase change occurs during the first charge. Due to the exceedingly low electrochemical performance of these materials as Li-ion battery cathodes, they are not likely to be of interest without significant differences in composition and preparation.

3.3 OXYGEN EVOLUTION CATALYTIC PERFORMANCE

A recent report[56] on the utility of $LiCoO_2$ as a catalyst for the OER prompted an OER screening of the materials that were prepared and characterized during the course of this study. A mass activity screening was performed first (Figure 3.5).

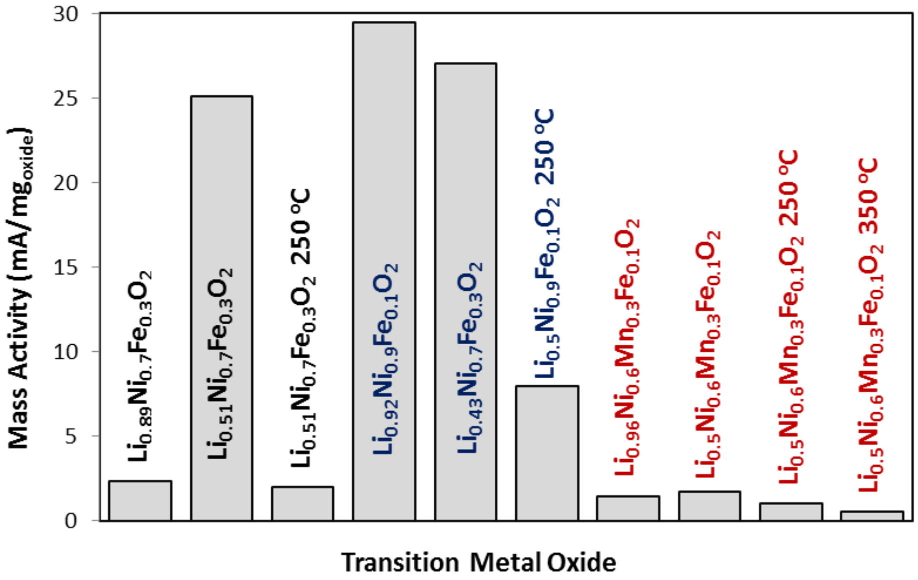

Figure 3.5 Mass activities of several oxides in the oxygen evolution reaction at E = 0.6 V vs. SCE.

Although this summary of catalytic activity does not account for differences in catalyst particle surface area, it does provide a few interesting results. For instance, all materials containing manganese show low activity. As a result, these materials were not pursued further. Additionally, $Li_{0.92}Ni_{0.9}Fe_{0.1}O_2$ shows the highest mass activity of all the samples tested. This is particularly significant in light of the fact that the near-stoichiometric Li materials have a significantly lower surface area than their delithiated and delithiated/annealed counterparts as determined by BET analysis (Table 3.2).

Table 3.2 BET surface areas of selected samples.

Sample	***BET Surface Area (cm^2 mg^{-1})***
$Li_{0.89}Ni_{0.7}Fe_{0.3}O_2$	3.72
$Li_{0.51}Ni_{0.7}Fe_{0.3}O_2$	34.72
$Li_{0.51}Ni_{0.7}Fe_{0.3}O_2$ 250 °C	63.87
$Li_{0.92}Ni_{0.9}Fe_{0.1}O_2$	7.12
$Li_{0.43}Ni_{0.9}Fe_{0.1}O_2$	39.15
$Li_{0.5}Ni_{0.9}Fe_{0.1}O_2$ 250 °C	192.37
$Li_{0.76}Ni_{0.8}Fe_{0.2}O_2$	18.00
$Li_{0.89}Ni_{0.95}Fe_{0.05}O_2$	7.80
$Li_{0.49}NiO_2$	20.80
NiO	34.63

BET analysis also demonstrates that annealing at 250 °C does not decrease surface area. In fact, post-delithitation annealing appears to have increased the surface area. This is likely due to intermediate grinding steps that were performed on the powders. While $Li_{0.51}Ni_{0.7}Fe_{0.3}O_2$ was gently ground in between delithiation and annealing, $Li_{0.43}Ni_{0.9}Fe_{0.1}O_2$ was mixed with a small amount of $Li_{0.92}Ni_{0.9}Fe_{0.1}O_2$ to achieve a Li stoichiometry of 0.5 and ground well for several minutes to achieve homogeneity. This may account for the significantly larger surface area of the heat-treated $Li_{0.5}Ni_{0.9}Fe_{0.1}O_2$ sample. Due to the ease with which grinding the powders increases their surface areas, it is likely that they are composed of small particles that are lightly sintered together into larger aggregates. If this is the case, it is unknown whether sonication during catalyst ink preparation or OER cycling in the alkaline electrolyte modifies the surface area. SEM investigations are in progress to address this issue. While electrochemical surface area (ECSA) measurements were performed according to the method of McCrory and Jaramillo[57] in 1 M KCl electrolyte, the measured double layer currents were almost identical for all samples. This is likely due to the low surface areas of the active materials. As a result, the double-layer currents of the catalyst materials could not be distinguished from those due to the acetylene black conductive additive, which has been observed previously.[58]

To correct for large differences in surface area, CVs of these materials are plotted using BET surface area-corrected current densities in Figure 3.6. Both the forward and reverse scans are plotted for all samples. The most striking feature in these CVs is the considerably lower potential at which $Li_{0.92}Ni_{0.9}Fe_{0.1}O_2$ generates a significant current. While significant O_2 evolution begins to occur at around 0.52 V vs. SCE for $Li_{0.92}Ni_{0.9}Fe_{0.1}O_2$, $Li_{0.89}Ni_{0.7}Fe_{0.3}O_2$ does not show meaningful catalytic activity until 0.6 V vs. SCE. Moreover, chemical delithiation drastically reduces catalytic activity per unit surface area. This effect is even more prominent when the delithiated samples are annealed at 250 ^{o}C to promote a phase change to a spinel-like phase. Although the delithiated samples and the delithiated/heated samples clearly show bulk structural changes as evidenced by their XRD patterns, it remains to be determined how their surface structures and chemistries differ. Raman spectroscopy or transmission electron microscopy may aid in this determination.

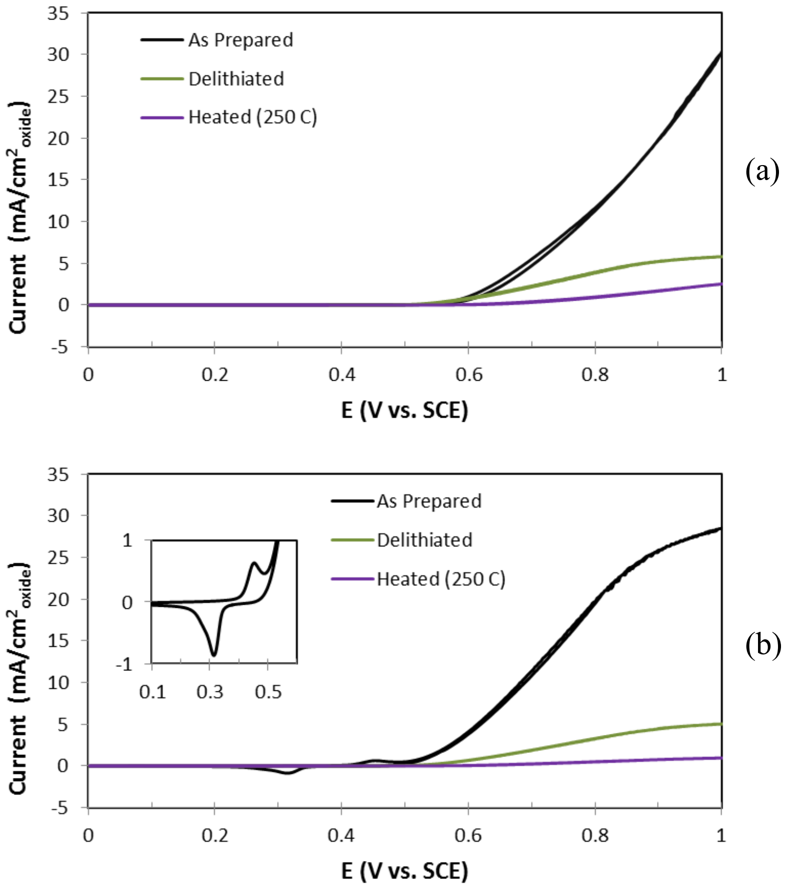

Figure 3.6 OER cyclic voltammograms of (a) $Li_xNi_{0.7}Fe_{0.3}O_2$ and (b) $Li_xNi_{0.9}Fe_{0.1}O_2$ series of materials.

Interestingly, $Li_{0.92}Ni_{0.9}Fe_{0.1}O_2$ is the only sample tested that displays any visible redox activity before the onset of O_2 evolution, as indicated by the small peaks present in the 0.2-0.5 V range. This feature is magnified in the inset in Figure 3.6(b), and it is attributed to the $Ni^{2+/3+}$ redox couple. Due to the significant influence of Fe content in the catalytic activity of Fe-substituted $LiNiO_2$, an investigation of this trend was completed. Accordingly, $Li_xNi_{1-y}Fe_yO_2$ (y = 0, 0.05, 0.1, 0.2, and 0.3) samples were prepared in the same manner and tested for the OER. The mass and specific activities (based on BET) are summarized in Figure 3.7.

Each composition was tested three times with a new electrode casting each time to ensure repeatability and minimize variations due to electrode film quality. The error bars in Figure 3.7 represent one standard deviation in both the positive and negative directions. NiO was also prepared in the same way and included for a comparison as it has been shown to be a competent OER catalyst in alkaline electrolytes.[59,60] These results show a significant increase in catalytic activity upon incorporation of Fe into layered $LiNiO_2$. In addition, there is a clear indication that a Fe content of approximately 10% results in the highest activity at moderate overpotentials. A Fe content of 5% shows slightly reduced activity, while Fe contents of 20% and 30% result in dramatically decreased activity.

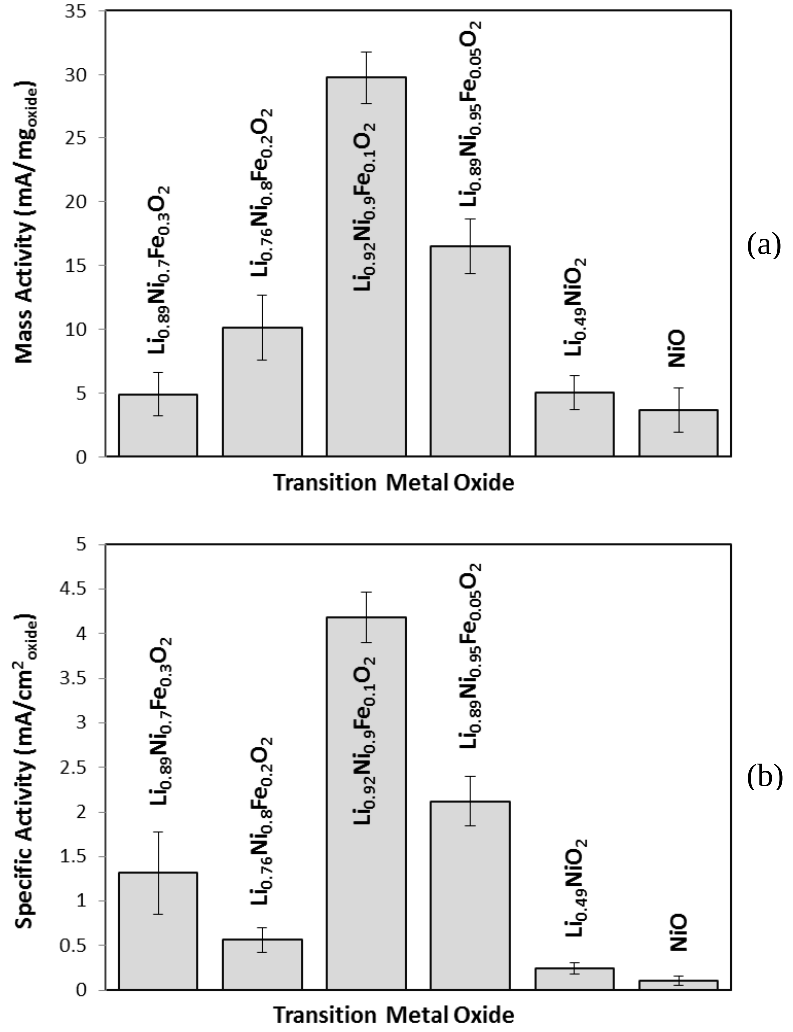

Figure 3.7 (a) Mass activities and (b) specific activities of the $Li_xNi_{1-y}Fe_yO_2$ series of oxides for the oxygen evolution reaction at 0.6 V vs. SCE.

These results are consistent with those of two recent studies on oxides containing Ni and Fe in alkaline electrolytes. Kitchin and coworkers prepared mixed Fe-Ni oxide catalysts by three different methods and observed a peak in catalytic performance near 10 % Fe content for all of them.[60] Using XRD, they established the presence of both NiO and $NiFe_2O_4$ phases at Fe concentrations below 25% and the formation of an additional phase (Fe_2O_3) at higher concentrations. The presence of $NiFe_2O_4$ was validated by Raman spectroscopy, and the authors attribute this phase to enhanced catalytic activity.

Boettcher and coworkers found that 10% Fe was the optimal concentration in $Ni_{1-x}Fe_xOOH$ oxyhydroxide electrocatalysts.[61] Although they found Fe incorporation to increase film conductivity 30-fold, this could not solely explain the marked increase in activity. They attribute the increase in catalytic activity to a partial charge transfer between Fe and Ni, producing Ni^{3+} with greater oxidizing power. This is evidenced by an anodic shift in the $Ni^{2+/3+}$ redox peaks upon increasing Fe content. In addition, combinatorial studies have shown that OER catalysts containing both Ni and Fe possess the highest activities. The incorporation of additional metals has comparably small effects on catalytic activity.[62,63]

It should be noted that the mass activities reported in Figure 3.7 were calculated from the second CV cycles in a series of three. While the second and third cycles are quite similar for all the samples tested, the first scan is significantly different for some of the samples. These differences are detailed in Figure 3.8. Figure 3.8a shows the first scan for all the samples. A prominent feature is the relatively large anodic $Ni^{2+/3+}$ peak for oxides containing 5 and 10% Fe. Although these redox waves are present for all three scans, the larger size of the first Ni^{2+} oxidation peak suggests irreversible extraction of Li^+. This has been reported to occur in $LiCoO_2$ upon oxidation of Co^{3+} to Co^{4+}.[56] In addition, samples containing 5 and 10% Fe show a significant voltage decrease in the onset of O_2 evolution between the first and second scans. In contrast, samples containing either more Fe or no Fe exhibit O_2 evolution at similar voltages in both scans. These observations suggest that Li^+ extraction is accompanied by *in situ* surface modification to afford a highly active OER catalyst.

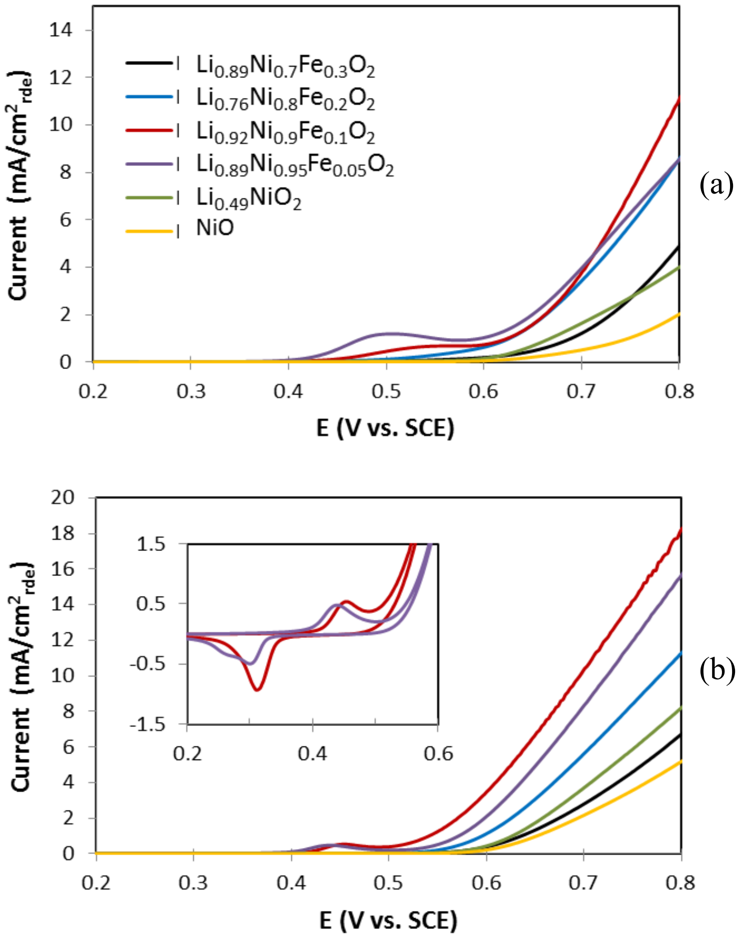

Figure 3.8 OER cyclic voltammograms of Fe-substituted layered $LiNiO_2$: (a) First sweep showing a large anodic peak for 5 and 10% Fe samples and (b) second sweep showing the enhanced activity of 5 and 10% Fe samples. Currents are normalized to the area of the rotating disc electrode (rde).

It is currently unknown how the catalyst surface is modified during multiple potential sweeps. Surface-sensitive characterization techniques such as x-ray photoelectron spectroscopy and Raman spectroscopy may elucidate the morphological and chemical changes that result in enhanced catalytic activity. It is possible that, despite significant differences in the bulk structure between Fe substituted nickel oxides, nickel oxyhydroxides, and layered lithium nickel oxides, their surfaces are structurally and chemically similar after potential sweeps in alkaline media. Alternatively, the incorporation of Fe may prime Ni for enhanced OER activity while the surfaces of these materials remain distinctly different. The results presented in this study emphasize the importance of elucidating the nature of the active catalyst during OER.

Chapter 4: Conclusions and Future Work

The major focus of this study was to synthesize a series Ni-rich layered oxides and determine how their chemical composition and structure affects their electrochemical properties in lithium-ion batteries and catalytic properties in the oxygen evolution reaction. To this end, a number of layered oxides containing Li, Ni, Fe, and/or Mn were synthesized. Some were chemically delithiated to remove half of the Li. The delithiated samples were also annealed at moderate temperatures to afford spinel-like phases. Elemental composition was determined by ICP-OES, and structures were studied using Rietveld refinement of their XRD patterns. The lattice parameters of known materials were found to be consistent with those in the literature. Moreover, delithiation was found to decrease **a** and increase **c** in the hexagonal layered structures.

While layered cathodes were found to result in rapid capacity fade upon cycling, spinel-like cathodes were found to possess very little reversible capacity. One composition, $Li_{0.5}Ni_{0.6}Mn_{0.3}Fe_{0.1}O_2$ heated to 250 ^{o}C, did have a voltage plateau in the 4.5 V region corresponding to spinel, but it suffered from low capacity after initial charging. These materials were deemed to have low practical use as cathodes in Li-ion batteries.

In the oxygen evolution reactions conducted in alkaline medium, layered oxides containing significant amounts of Mn were found to have low catalytic activity. In contrast, $Li_{0.92}Ni_{0.9}Fe_{0.1}O_2$ showed significantly higher activity than the other samples initially tested. It also showed redox peaks corresponding to the $Ni^{2+/3+}$ couple. This lead prompted an investigation of $Li_{\sim1}Ni_{1-x}Fe_xO_2$ ($0 < x < 0.3$) to determine the effect of Fe substitution on OER catalysis. $Li_xNi_{1-y}Fe_yO_2$ ($y = 0, 0.05, 0.1, 0.2,$ and 0.3) samples were prepared in the same manner and tested for the OER. It was found that a Fe content of approximately 10% results in the highest OER activity, with decreased activities for both larger and smaller Fe contents. The similarity between these results and those found with other Fe substituted nickel oxides suggests either a similar surface morphology upon cycling or a similar electronic enhancement of Ni OER activity upon Fe substitution. Further studies of the surfaces of these oxides are warranted.

References

1. U.S. Energy Information Administration. International Energy Outlook 2013. http:// http://www.eia.gov/forecasts/ieo/index.cfm (accessed Mar 26, 2014).
2. U.S. Energy Information Administration. Few transportation fuels surpass the energy densities of gasoline and diesel. http://www.eia.gov/todayinenergy/detail.cfm?id=9991 (accessed Mar 26, 2014).
3. Denholm, P.; Margolis, R. M. *Energy Policy* **2007**, *35*, 2852.
4. Whittingham, M. S. *Science* **1976**, *192*, 1126.
5. Mizushima, K.; Jones, P. C.; Wiseman, P. J.; Goodenough, J. B. *Mater. Res. Bull.* **1980**, **15**, 783.
6. Yazami, R.; Touzain, P. *J. Power Sources* **1983**, *9*, 365.
7. Yoshino, A.; Kenichi, S.; Takayuki, N. Secondary Battery. U.S. Patent 4,668,595, May 26, 1987.
8. Park, O. K.; Cho, Y.; Lee, S.; Yoo, H.-C.; Song, H.-K.; Cho, J. *Energy Environ. Sci.* **2011**, *4*, 1621.
9. Manthiram, A. Materials Aspects: An Overview. In *Lithium Batteries: Science and Technology*; Nazri, G.-A. and Pistoia, G., Eds.; Springer: New York, 2003; pp 2-41.
10. Manthiram, A. Battery Applications. In *Encyclopedia of Smart Materials*; Schwartz, M., Ed.; Wiley: New York, 2002; Vol. 1; pp 68-82.
11. Goodenough, J. B.; Kim, Y. *Chem. Mater.* **2010**, **22**, 587.
12. Pistoia, G., Ed. *Lithium-Ion Batteries: Advances and Applications*; Elsevier: Amsterdam, 2014.
13. Structures prepared with VESTA Software, http://jp-minerals.org/vesta/en/.
14. Mendiboure, A.; Delmas, C.; Hagenmuller, P. *Mater. Res. Bull.* **1984**, *19*, 1383.

15. Chebiam, R. V.; Prado, F.; Manthiram, A. *Chem. Mater*. **2001**, *13*, 2951.
16. Chebiam, R. V.; Prado, F.; Manthiram, A. *J. Solid State Chem*. **2002**, *163*, 5.
17. Rougier, A.; Gravereau, P.; Demlas, C. *J. Electrochem. Soc*. **1996**, *143*, 1168.
18. Kalyani, P.; Kalaiselvi, N. *Sci. Tech. Adv. Mater*. **2005**, *6*, 689.
19. Thackeray, M. M.; David, W. I. F.; Bruce, P. G.; Goodenough, J. B. *Mater. Res. Bull*. **1983**, *18*, 461.
20. Thackeray, M. M.; David, W. I. F.; Bruce, P. G.; Goodenough, J. B. *Mater. Res. Bull*. **1984**, *19*, 179.
21. Thackeray, M. M.; Mansuetto, M. F.; Dees, D. W.; Vissers, D. R. *Mater. Res. Bull*. **1996**, **31**, 133.
22. Kim, J.; Manthiram, A. K. *J. Electrochem Soc*. **1998**, *145*, L53.
23. Sigala, C.; Guyomard, D.; Verbaere, A.; Piffard, Y.; Tournoux, M. *Solid State Ionics* **1995**, *81*, 167.
24. Zhong, Q.; Bonakdarpour, A.; Zhang, M.; Gao, Y.; Dahn, J. R. *J. Electrochem. Soc*. **1997**, *144*, 205.
25. Thomas, M. G. S. R.; David, W. I. F.; Goodenough, J. B. *Mat. Res. Bull*. **1985**, *20*, 1137-1146.
26. Choi, S.; Manthiram, A. *J. Electrochem. Soc*. **2002**, *149*, A1157.
27. Choi, S.; Manthiram, A. *J. Solid State Chem*. **2002**, *164*, 332.
28. Choi, S.; Manthiram, A. *J. Electrochem. Soc*. **2002**, *149*, A162.
29. Lee, K.-K.; Yoon, W.-S.; Kim, K.-B.; Lee, K.-Y.; Hong, S.-T. *J. Electrochem. Soc*. **2001**, *148*, A716.
30. Dutta, G.; Manthiram, A.; Goodenough, J. B. *J. Solid State Chem*. **1992**, *96*, 123.

31. Chazel, C.; Menetrier, M.; Carlier, D.; Croguennec, L.; Delmas, C. *Chem. Mater*. **2007**, *19*, 4166.
32. Kanno, R.; Kubo, H.; Kawamoto, Y. *J. Solid State Chem*. **1994**, *110*, 216.
33. Vidyasagar, K.; Gopalakrishnan, J. *J. Solid State Chem*. **1982**, *42*, 217.
34. de Picciotto, L. A.; Thackeray, M. M. *Mater. Res. Bull*. **1985**, *20*, 1409.
35. de Picciotto, L. A.; Thackeray, M. M. *Solid State Ionics* **1986**, *18-19*, 773.
36. de Picciotto, L. A.; Thackeray, M. M. *Mater. Res. Bull*. **1984**, *19*, 1497.
37. de Picciotto, L. A.; Thackeray, M. M. *Mater. Res. Bull*. **1985**, *20*, 187.
38. Kim, S.; Ma, X.; Ong, S. P.; Ceder, G. *Phys. Chem. Chem. Phys*. **2012**, *14*, 15571.
39. Ma, X.; Hautier, G.; Jain, A.; Doe, R.; Ceder, G. *J. Electrochem. Soc*. **2013**, *160*, A279.
40. Christensen, J.; Albertus, P.; Sanchez-Carrera, R. S.; Lohmann, T.; Kozinsky, B.; Liedtke, R.; Ahmed, J.; Kojic, A. *J. Electrochem. Soc*. **2012**, *159*, R1.
41. Ferrara, F. PhD. Dissertation, University of Cagliari, 2008.
42. Chemelewski, W. D.; Lee, H.-C.; Lin, J.-F.; Bard, A. J.; Mullins, C. B. *J. Am. Chem. Soc.* **2014**, *136*, 2843-2850.
43. Koper, M. T. M. *J. Electroanal. Chem*. **2011**, *660*, 254.
44. Man, I. C.; Su, H.-Y.; Calle-Vallejo, F.; Hansen, H. A.; Martinez, J. I.; Inoglu, N. G.; Kitchin, J.; Jaramillo, T. F.; Norskov, J. K.; Rossmeisl, J. *ChemCatChem* **2011**, *3*, 1159.
45. Garcia, E. M.; Taroco, H. A.; Matencio, T.; Domingues, R. Z.; dos Santos, J. A. F. *Int. J. Hydrogen Energy* **2012**, *37*, 6400-6406.
46. Suntivich, J.; May, K. J.; Gasteiger, H. A.; Goodenough, J. B.; Shao-Horn, Y. *Science* **2011**, *334*, 1383.

47. Singh, R. N.; Pandey, J. P.; Singh, N. K.; Lal, B.; Chartier, P.; Koenig, J. F. *Electrochim. Acta* **2000**, *45*, 1911.
48. Da Silva, L. M.; Boodts, J. F. C.; De Faria, L. A. *Electrochim. Acta* **2001**, *46*, 1369.
49. Guo, X.; Greenbaum, S.; Ronci, F.; Scrosati, B. *Solid State Ionics* **2004**, *168*, 37.
50. Fullprof Suite. https://www.ill.eu/sites/fullprof/ (downloaded 2013).
51. PDXL: Integrated X-ray powder diffraction software, Rigaku.
52. Hou, X.; Jones, B. T. Inductively Coupled Plasma/Optical Emission Spectrometry. In *Encyclopedia of Analytical Chemistry*; Meyers, R. A., Ed; Wiley: Chichester, 2003; pp 1-17.
53. Prado, G.; Rougier, A.; Fournes, L.; Delmas, C. *J. Electrochem. Soc*. **2000**, *147*, 2880.
54. McCusker, L. B.; Von Dreele, R. B.; Cox, D. E.; Louer, D.; Scardi, P. *J. Appl. Cryst*. **1999**, *32*, 36.
55. Reimers, J. N.; Rossen, E.; Jones, C. D.; Dahn, J. R. *Solid State Ionics* **1993**, *61*, 335.
56. Lee, S. W.; Carlton, C.; Risch, M.; Surendranath, Y.; Chen, S.; Furutsuki, S.; Yamada, A.; Nocera, D. G.; Shao-Horn, Y. *J. Am. Chem. Soc*. **2012**, *134*, 16959.
57. McCrory, C. C. L.; Jung, S.; Peters, J. C.; Jaramillo, T. F. *J. Am. Chem. Soc*. **2013**, *135*, 16977.
58. Chen, J. Y. C.; Miller, J. T.; Gerken, J. B.; Stahl, S. S. *Energy Environ, Sci*. **2014**, *7*, 1382.
59. Yeo, B. S.; Bell, A. T. *J. Phys. Chem. C* **2012**, *116*, 8394.
60. Landon, J.; Demeter, E.; Inoglu, N.; Keturakis, C.; Wachs, I. E.; Vasic, R.; Frenkel, A. I.; Kitchin, J. R. *ACS Catal*. **2012**, *2*, 1793.

61. Trotochaud, L.; Young, S. L.; Ranney, J. K.; Boettcher, S. W. *J. Am. Chem. Soc*. **2012**, Just Accepted Manuscript; DOI: 10.1021/ja502379c.
62. Haber, J. A.; Cai, Y.; Jung, S.; Xiang, C.; Mitrovic, S.; Jin, J.; Bell, A. T.; Gregorie, J. M. *Energy Environ. Sci*. **2014**, *7*, 682.
63. Xiang, C.; Suram, S. K.; Haber, J. A.; Guevarra, D. W.; Soedarmadji, E.; Jin, J.; Gregorie, J. M. *ACS Comb. Sci*. **2014**, *16*, 47.